

# QUASI-STATIC SINGLE-COMPONENT HYBRID SIMULATION OF A COMPOSITE STRUCTURE WITH MULTI-AXIS CONTROL

Jacob Høgh<sup>1</sup>, Jacob Waldbjørn<sup>2</sup>, Jacob Wittrup-Schmidt<sup>2</sup>, Henrik Stang<sup>2</sup> and Christian Berggreen<sup>1</sup>

<sup>1</sup>Department of Mechanical Engineering, Technical University of Denmark, Kgs. Lyngby, Denmark

<sup>2</sup>Department of Civil Engineering, Technical University of Denmark, Kgs. Lyngby, Denmark

**Keywords:** *single-component hybrid simulation, hardware-in-the-loop, sub-structural testing, composite structure, multi-axial control, finite element modelling, high-precision control*

## Abstract

This paper presents a quasi-static hybrid simulation performed on a single component structure. Hybrid simulation is a sub-structural technique, where a structure is divided into two sections: a numerical section of the main structure and a physical experiment of the remainder. In previous cases, hybrid simulation has typically been applied to structures with a simple connection between the numerical model and physical test, e.g. civil engineering structures. In this paper, the method is applied to a composite structure, where the boundary is more complex i.e. 3 degrees of freedom (DOF). In order to evaluate the validity of the method, the results are compared to a test of the emulated structure – referred to here as the reference test. It was found that the error introduced by compliance in the load train were significant. Digital Image Correlation (DIC) was for this reason implemented in the hybrid simulation communication loop to compensate for this source of error. Furthermore, the accuracy of the hybrid simulation was improved by compensating for communication delay. The test showed high correspondence between the hybrid simulation and the reference test in terms of overall deflection as well as displacements and rotation in the shared boundary.

## Introduction

The ambition to improve the structural and operational performance of large structures within the industry of wind energy [1] has resulted in extensive research regarding large scale- and high performance composite structures. In these efforts, testing has primary been focusing on two scales: full scale and coupon testing [2]. Full scale testing provides valuable knowledge of the structural behavior, but is time consuming and expensive to perform due to the large scale of the structure [1]. The structure is typically tested in simple load configuration which is a significant simplification of the actual loads to which the structure is exposed during service. In order to investigate the material characteristics of the individual materials in the composite structure, coupon testing is conducted [3]. Such tests are performed on specially designed specimens, resulting in idealized stress- and strain states and as a consequence, they do not account for the complex stress states and interactions between the different materials in the joints, bearings and other critical details throughout the structure.

To address shortcomings in full scale and material testing, the hybrid simulation concept is introduced. Hybrid simulation provides the capability to isolate and experimentally test a critical section of special interest for which a reliable analytical model may not be available. The remainder of the emulated structure is assumed to be well understood and is for that reason handled in a numerical model [4, 5]. As a

consequence, neither cost-intensive full-scale experiments nor demanding theoretical evaluation procedure is required to reveal the response of the experimental substructure, when exposed to the effect of the remaining structure. The coupling between the numerical and experimental substructure is governed through the interface between the two components referred to here as the shared boundary. During the test, a predefined external displacement is applied the numerical substructure which are equivalent to the loads acting on the structure during service. The corresponding response is computed through a commercial Finite Element (FE) software and imposed on the experimental substructure using actuators. The forces required to deform the experimental substructure – referred to here as the restoring force – are retrieved and fed back to the numerical substructure to compute the next displacement corresponding to the next time step. This communication is established through an algorithm, referred to here as the hybrid simulation communication loop.

The hybrid simulation technique originated in the late 1960's, where it was used for simulation of the structural response to an earthquake as an alternative to shake table test [6]. Since, the research within hybrid simulation has mainly been focused on seismic protection of building structures [7, 8]. Here the numerical and experimental substructure has been two separate – typically simply connected – structural components referred to here as multi-component hybrid simulation. For this application the load bearing structure has been simulated in a numerical model while damping fixtures has been tested experimentally e.g. elastomer [9], stud types, [10, 11] and magneto-rheological [12, 13]. However, to close the gap between full scale and material testing within the industry of wind energy, the hybrid simulation concept is implemented for a single component structure – referred to here as single component hybrid simulation. This complicates the transferring of response between the two substructures given that the shared boundary consists of an edge instead of e.g. a clearly defined hinge as presented in [14, 15]. This comprises an infinite number of contact points yielding a complex force/displacement distribution in the coupling between the two substructures. The operation of the shared boundary justifies the need for advanced measuring techniques to ensure a high degree of accuracy in the displacement imposed on the shared boundary of the experimental substructure [16, 17]. To the author's knowledge, only a single publication is published concerning single-component hybrid simulation [18]. Here the concept is introduced and the system demonstrated on a composite beam with the shared boundary covering a discrete point with a single Degrees-of-freedom (DOF).

The scope of this paper is to perform a single-component hybrid simulation – here with special attention paid to the operation of the shared boundary between the numerical and experimental substructure. The emulated structure consists of a composite beam, clamped in both ends and loaded by a single point load. The shared boundary is described as a discrete point with three DOF's. Digital Image Correlation (DIC) is implemented as a method of adjusting the quasi-static imposed displacements on the shared boundary, to fit the command signal received by the numerical model – referred to here as a *DIC Compensator*. Furthermore, compensation of communication delay is conducted through linear regression – referred to here as a *Communication Delay Compensator*. A parametric study is conducted where the effect of: DIC compensation and Communication delay compensation is investigated. Finally the optimal configuration of these two parameters is identified and demonstrated on an applied case. For verification of the single-component hybrid simulation technique a test of the emulated structure is conducted – referred to here as the reference test. Here a point load is applied the specimen and the global response monitored in multiple measurement point to compare with the global response of the hybrid simulation.

## Hybrid Simulation Setup

The reference structure consists of a beam which is clamped in both ends and loaded by an external displacement  $D_{ext}$  cf. Fig. 1. This test configuration is studied to reduce the complexity in verifying the hybrid simulation communication loop capabilities and operation of the shared boundary. The material properties of the reference structure are determined by coupon testing cf. Table 1.

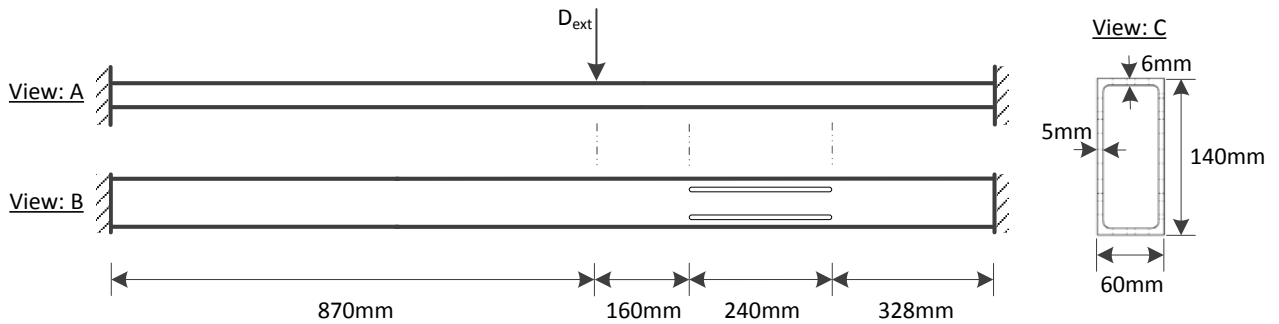


**Fig. 1 Reference structure representing the overall dimensions, external displacement and boundary conditions**

The reference structure is separated in a numerical- and experimental substructure. Two slits are located in the top flange in order to yield a geometrical non-linear response of the experimental substructure due to buckling. This effect is triggered by two slits in the compression flange cf. Fig. 1b. Each substructure along with the coupling between them is illustrated in Fig. 2.

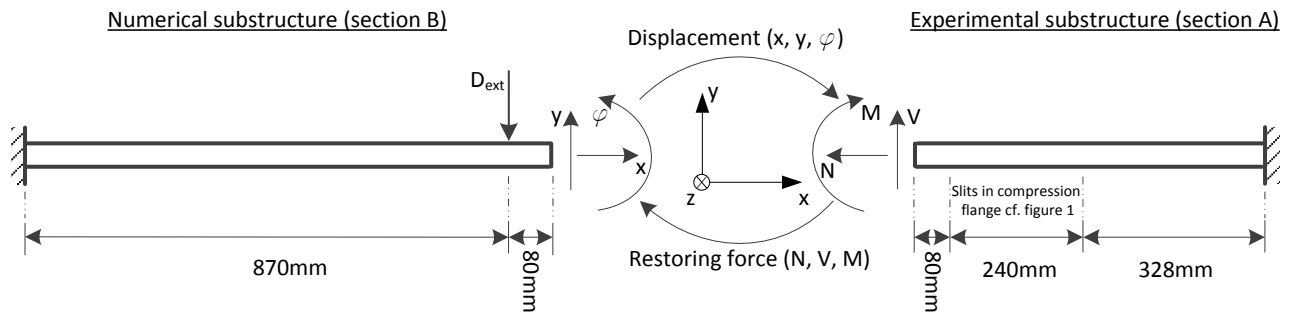


**Fig. 2 The reference structure separated in: a) numerical substructure and b) experimental substructure**

The shared boundary between the two substructures is defined by a discrete point with three DOFs: translation in the  $x$ - and  $y$ -direction along with rotation around the  $z$ -axis – referred to here as  $\varphi$ .

### *Experimental Substructure (Section A)*

The experimental substructure consists of a 648mm long thin-walled Glass Fiber Reinforced Polymer (GFRP) beam produced by Fiber Pultrusion. The closed rectangular cross section has a width and height of 140mm and 60mm respectively, while the corresponding material thickness is 5mm and 6mm cf. Fig. 1c. Two slits at the center of the compression flange is initiated in order to include non-linear behavior. These slits are located 112 mm from each other, each with a length and width of 240 and 4 mm respectively. The experimental substructure is loaded as a cantilever beam, with the free edge as the shared boundary between

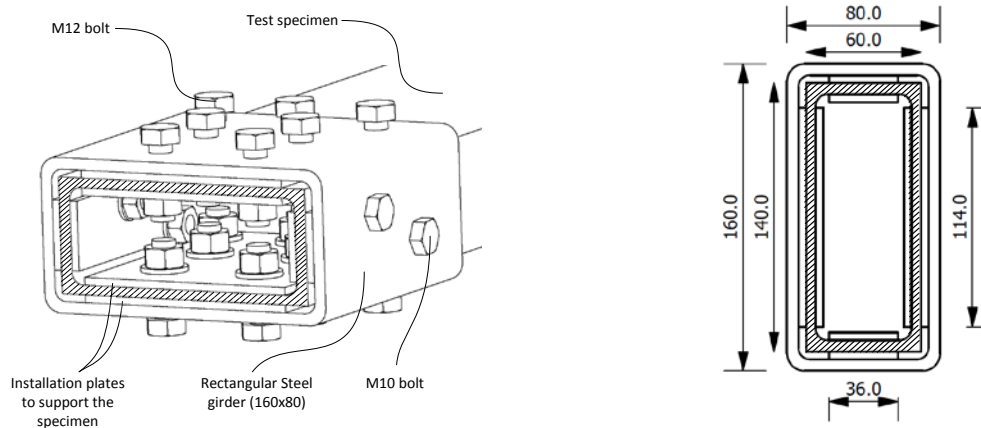
the two substructures cf. Fig. 2. The in-plane material properties of the tensile/compression flange are presented in Table 1, determined in accordance with D3039/D3039M – 08 [19] and D5379/D5379M – 12 [20].

**Table 1: In-plane tensile moduli, shear modulus and poisons ratio**

| Spec. [-]                   | $E_1$ [GPa] | $E_2$ [GPa] | $\nu_{12}$ [-] | $\nu_{21}$ [-] | $G_{12}$ [GPa] | $G_{21}$ [GPa] |
|-----------------------------|-------------|-------------|----------------|----------------|----------------|----------------|
| 1                           | 34.79       | 10.09       | 0.23           | 0.07           | 3.49           | 3.10           |
| 2                           | 25.48       | 9.24        | 0.23           | 0.08           | 3.64           | 2.75           |
| 3                           | 21.68       | 9.31        | 0.22           | 0.09           | 3.56           | 3.03           |
| 4                           | 20.89       | 10.17       | 0.21           | 0.07           | 3.18           | 3.38           |
| 5                           | 23.65       | 10.52       | 0.24           | 0.09           | 3.59           | 2.85           |
| 6                           | 32.41       | 9.91        | 0.22           | 0.07           | 3.08           | 3.25           |
| 7                           | 39.63       | 10.49       | 0.25           | 0.08           | 3.39           | -              |
| 8                           | -           | -           | -              | -              | 3.33           | -              |
| Average                     | 28.36       | 9.96        | 0.23           | 0.08           | 3.41           | 3.06           |
| Standard deviation          | 7.25        | 0.52        | 0.01           | 0.01           | 0.20           | 0.24           |
| Coefficient of variance [%] | 25.57       | 5.18        | 5.89           | 11.45          | 5.90           | 7.75           |

The tensile stress-strain relation in both the 1- and 2-direction is demonstrated linear elastic until failure. For the longitudinal tensile specimen a clear relation between the laminate stiffness and position in the width of the tension /compression flange (2-direction) is observed. The lowest stiffness is found at the center of the tensile/compression flange while increasing when moving towards the corner of the cross section. This tendency is most likely caused by variances in the fiber content along the width of the tension/compression flange.

The specimen is in both ends clamped to the rig through a rectangular steel profile cf. Fig. 5. Installation plates of steel are positioned on each side of the test specimen for supporting and to avoid critical stress concentrations in the interface between the test specimen and rectangular steel profile. Everything is tightened together by eighteen bolts to establish a stiff friction connection between the rectangular steel profile and test specimen, see Fig. 3.



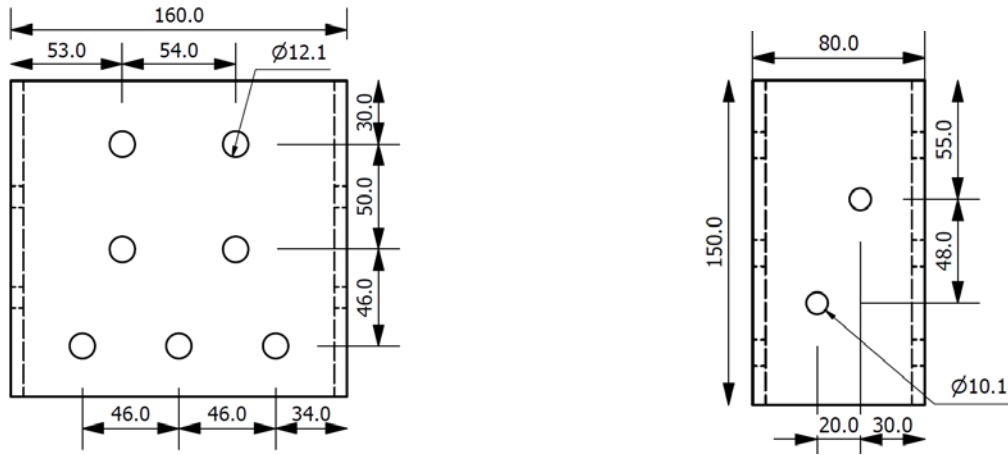


**Fig. 3 Clamped support of the experimental substructure**

### *Numerical Substructure (Section B)*

The numerical substructure is simulated in ANSYS 15.0 in a 3D FE-model, using 8-node shell elements of the type: shell281. Each side of the shell element includes a node in the corner and middle. These elements have 6 DOFs in each node: translation and rotation in the  $x$ -,  $y$ -, and  $z$ -direction. The model has 2256 elements and orthotropic material properties are assigned according to Table 1. The  $G$ -moduli are taken as the average of the  $G_{12}$  and  $G_{21}$  for all directions for simplicity. The same assumption is made for the Poisson's ratio.

**Table 2: Orthotropic material properties used in the finite element model**

| $E_x$ [GPa] | $E_y$ [GPa] | $E_z$ [GPa] | $G_{xy}$ [GPa] | $G_{yz}$ [GPa] | $G_{xz}$ [GPa] | $\nu_{xy}$ [-] | $\nu_{yz}$ [-] | $\nu_{xz}$ [-] |
|-------------|-------------|-------------|----------------|----------------|----------------|----------------|----------------|----------------|
| 28.36       | 9.96        | 9.96        | 3.235          | 3.235          | 3.235          | 0.155          | 0.155          | 0.155          |

The external displacement is applied the numerical structure as nodal displacement along a line 870mm from the clamped support, cf. Fig. 1.

The restoring force is applied the structure at the position of 950mm from the support, Fig. 2. The vertical- and horizontal forces and moment are applied as nodal loads. The nodal loads are distributed statically and work equivalent to the uniformly distributed forces and moments in the structure.

The clamped supports of the finite element model are designed as presented in Fig. 4 with a width, height and thickness of 160x280x10mm and isotropic material properties. To ensure an identical stiffness of the numerical and experimental clamped support, a FE model of the reference structure is created. Here the Young's modulus,  $E$ , of the support in the finite element model is adjusted to fit the root rotation of the composite beam measured in the test of the reference structure. This rotation is measured by DIC in MP 12, 13 and 14 cf. Fig. 7. The correct rotation occurred with a Young's modulus of 170GPa.

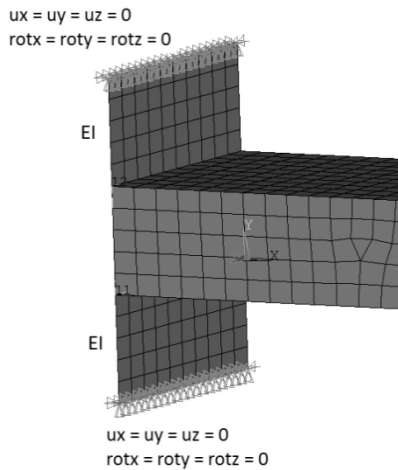


**Fig. 4 The clamped support of the finite element model**

### Experimental Test Setup

The experimental test setup is handled in a suitably stiff frame structure, re-configurable to handle both the reference test, see Fig. 7 and experimental substructure of the hybrid simulation, see Fig. 5. Fabricated steel interface plates are mounted to the frame structure to accommodate the swivel base of up to three servo-hydraulic actuators named A, B and C. Actuator A is a MTS model: 244.12 which provide a force capacity of  $\pm 25\text{kN}$  with a static and dynamic stroke of 182.9mm and 152.4mm respectively. The actuator is operated by a servo valve model: MTS 252.23G-01 with a capacity of 19l/min. The displacement of the actuator is monitored by a Linear Variable Differential Transducer (LVDT) and the force measured by an MTS load cell model: 661.19E-04 with a capacity of  $\pm 25\text{kN}$ . Actuator B and C is a MTS model: 242.01 which provide a force capacity of  $\pm 5\text{kN}$  with a static and dynamic stroke of 114.3 and 101.6mm respectively. The actuator is operated by a servo valve model: MTS 252.21G-01 with a capacity of 4l/min. The displacement of the actuator is monitored by a LVDT and the force measured by an MTS load cell model: 661.19E-01 with a capacity of  $\pm 5\text{kN}$ . The actuators are operated through a MTS TestStar II PID – controller with a three channel configuration. The system is connected to a hydraulic power unit (HPU) operating at 3000psi pressure.

### Experimental Substructure of the Hybrid Simulation

The experimental substructure of the hybrid simulation consists of the cantilever GFRP beam loaded in the stiff frame structure, described above, by three actuators A, B and C cf. Fig. 5. The response of the GFRP beam is monitored on both lateral sides by two individual 3D - DIC systems named: DIC 1 and DIC 2. The camera setup and performance of the DIC system are presented in Table 3.

**Table 3 Setup and performance of the 3D-DIC system**

| Configuration label | Hybrid Simulation      |                         | Reference Test         |                         |
|---------------------|------------------------|-------------------------|------------------------|-------------------------|
|                     | DIC 1                  | DIC 2                   | DIC 3                  | DIC 4                   |
| Technique used      | 3D image correlation   | 3D image correlation    | 3D image correlation   | 3D image correlation    |
| Subset              | 20 pixel               | 20 pixel                | 20 pixel               | 20 pixel                |
| Shift               | 13 pixel               | 13 pixel                | 13 pixel               | 13 pixel                |
| Camera Lens         | 4M 1" CCD chip<br>20mm | 2M 2/3" CCD chip<br>8mm | 4M 1" CCD chip<br>20mm | 2M 2/3" CCD chip<br>8mm |

|                      |                                       |                                       |                                       |                                       |
|----------------------|---------------------------------------|---------------------------------------|---------------------------------------|---------------------------------------|
| Field of View        | 2048 x 2048 pixel                     | 1600 x 1200 pixel                     | 960mm x 960mm<br>2048x2048pixel       | 590mm x 590mm<br>1600x1200pixel       |
| Measurement points   | 24818                                 | 11360                                 | 24818                                 | 11360                                 |
| <b>Displacement</b>  |                                       |                                       |                                       |                                       |
| Spatial resolution   | 20 pixel                              | 20 pixel                              | 20 pixel                              | 20 pixel                              |
| Resolution, $\sigma$ |                                       |                                       |                                       |                                       |
| Standard dev.        |                                       |                                       |                                       |                                       |
| In-plane             | 5.1 $\mu\text{m}$ x 3.5 $\mu\text{m}$ | 6.6 $\mu\text{m}$ x 3.4 $\mu\text{m}$ | 4.1 $\mu\text{m}$ x 3.4 $\mu\text{m}$ | 5.6 $\mu\text{m}$ x 3.2 $\mu\text{m}$ |
| Out-of-plane         | 21.7 $\mu\text{m}$                    | 17.2 $\mu\text{m}$                    | 17.8 $\mu\text{m}$                    | 17.0 $\mu\text{m}$                    |

From the DIC measurements the displacement of the sheared boundary and remainder of the experimental substructure is tracked through five measurement points (MP) on each side cf. Fig. 5. Given that the measurement points for DIC 1 are tracked real-time, no full field data is available from this system, due to software limitations. Both sides of the GFRP beam is applied a high contrast by a random speckle pattern of white background with black dots. The surface is illuminated with an even and high intensity. The compression and tension flanges are monitored through three strain gauge measurements (SG) on each side cf. Fig. 5. The electrical strain gauges are of the type SR-4 general purpose strain gauges from Vishay Micro-measurements. The gauge resistance is  $120.0\Omega \pm 0.3\%$  and gauge length 6.00mm with a gauge factor of  $2.075 \pm 0.5\%$  for all specimens. The test configuration along with position and numbering of the DIC and strain gauge measurement are presented in Fig. 5.

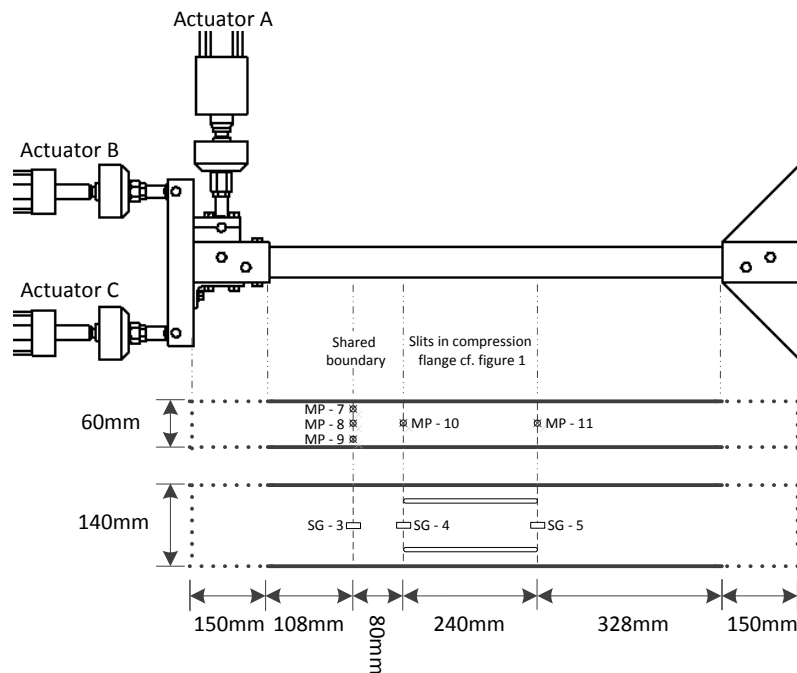


**Fig. 5 Experimental substructure including: test rig and specimen with MP and SG**

The three DOF's of the shared boundary is monitored through three measurement points named: MP7, MP8 and MP9 cf. Fig. 5. The shared boundary is located 108mm from the rectangular steel profile to erase any strain concentrations initiated by the clamped support. Through DIC compensation, the quasi-static imposed displacements at the shared boundary are adjusted to fit the command signal received by the numerical model [16]. The full setup of the test configuration including: hydraulic actuators, specimen mounted in the test rig, strain gauges and DIC camera is presented in Fig. 6.

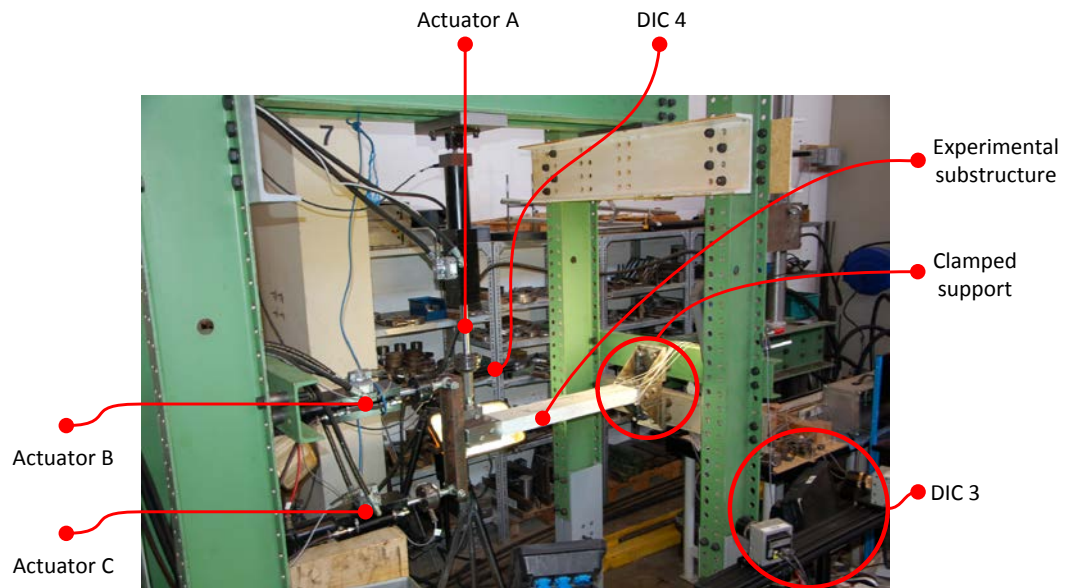


**Fig. 6 The multi-axial single-component hybrid simulation setup with GFRP beam, strain gauges and speckle pattern**

### *Reference Test*

The reference test consist of the GFRP beam, cf. Fig. 1, which is clamped in both ends and loaded in the stiff frame structure described above, by the servo-hydraulic actuator A cf. Fig. 7. The response of the GFRP is likewise monitored on both lateral sides by two individual 3D – DIC systems named: DIC 3 and DIC 4. The camera setup and performance of the DIC system is presented in Table 3. From the DIC measurements the displacement of the sheared boundary and remainder of the reference structure is tracked through fourteen measurement points (MP) on each side cf. Fig. 7. The compression and tension flanges are monitored through five strain gauge measurements (SG) on each side cf. Fig. 7. The electrical strain gauges are of the same type and specifications as the ones used in the experimental substructure of the hybrid simulation. The full test configuration along with position and numbering of the DIC and strain gauge measurement are presented in Fig. 7.

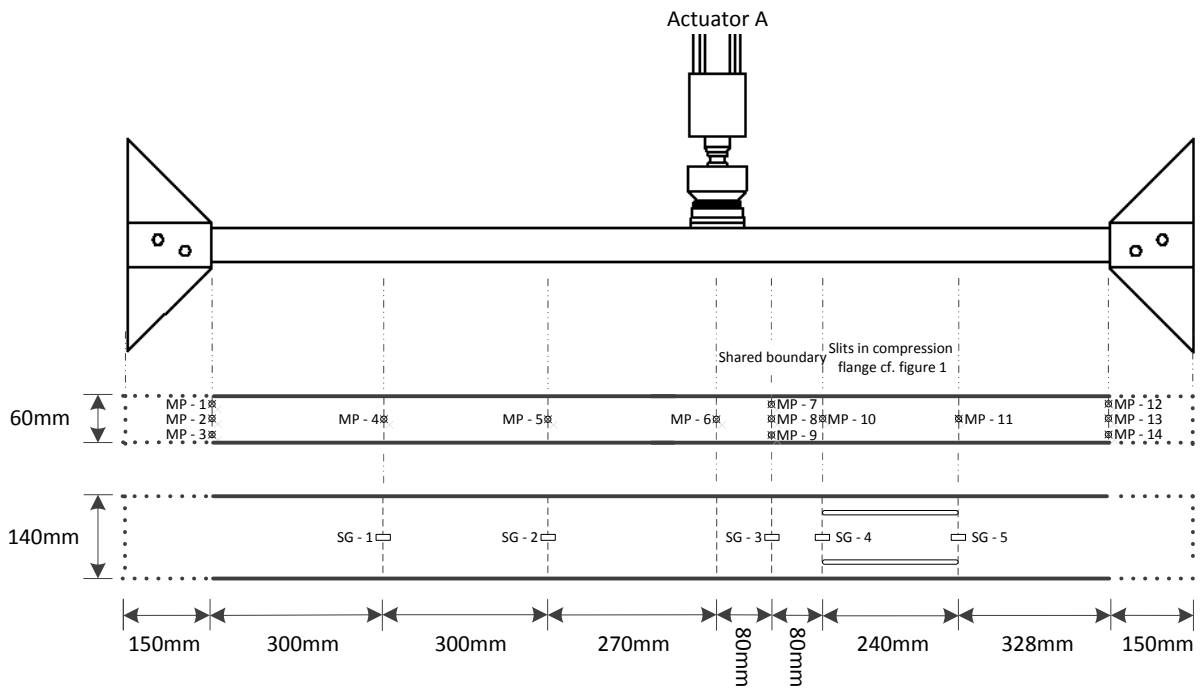


**Fig. 7 The test of the reference structure including: test rig and specimen with measurement points**

The specimen is in both ends clamped cf. Fig. 7. Details of the clamping support are given in Fig. 3. The full setup of the test configuration including: the hydraulic actuator, specimen mounted in the test rig and DIC camera is presented in Fig. 8.

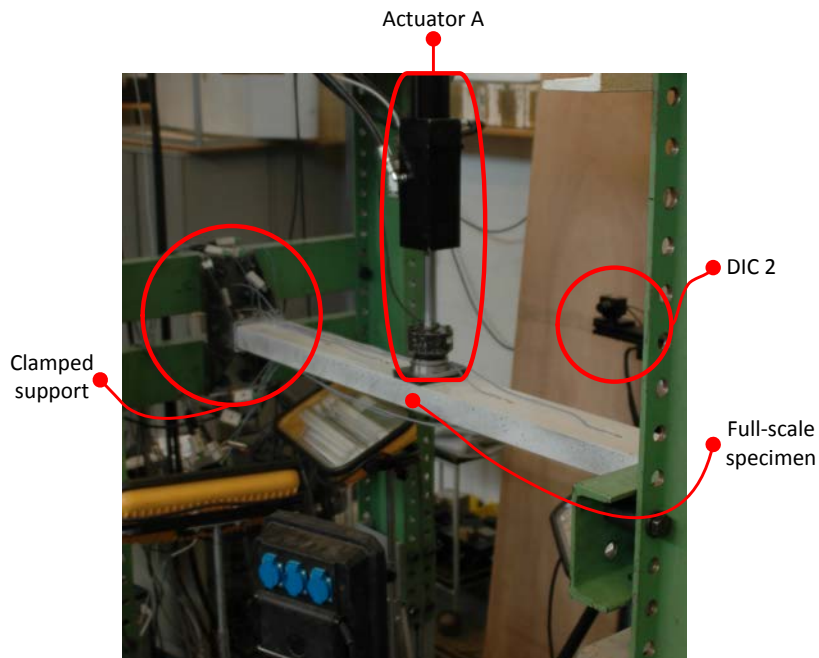


**Fig. 8 The reference test with GFRP beam, strain gauges and speckle pattern**

## Hybrid Simulation Communication Loop

The quasi-static hybrid simulation communication loop provides the capability to experimentally test a substructure of interest while simulating the remainder in a numerical model on an extended time scale. The software is partitioned in a numerical and experimental portion, connected through a digital to analogue - analogue to digital interface. The software is operated in a producer/consumer architecture [21] through LabVIEW 13.0. The outline of the dataflow in the hybrid simulation communication loop is presented in Fig. 9.

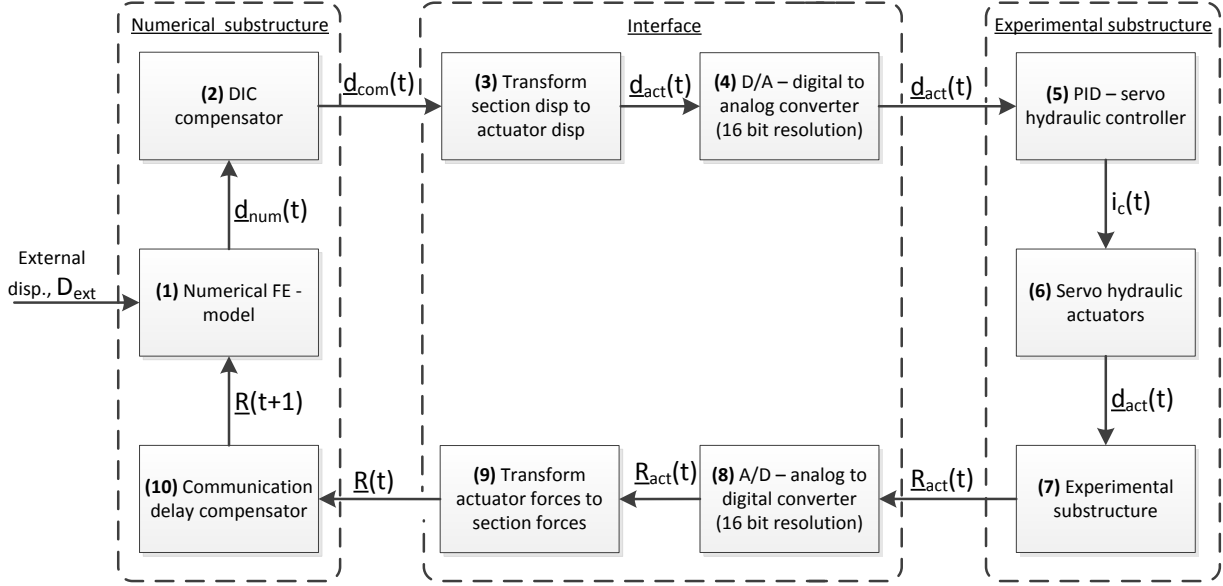


**Fig. 9 Dataflow in the quasi-static hybrid simulation communication loop**

The interface between the numerical and experimental substructure is generated through a NI9205 and NI9263 LabVIEW board. Product specifications including: accuracy and precision are stated in [22] and [23].

An external displacement is applied to the numerical FE-model (1) further clarified in Fig. 2. The FE-model is defined by the ANSYS Parametric Design Language (APDL-script) and executed in batch mode through the Windows command prompt. The displacement  $\underline{d}_{num}(t)$  at the shared boundary for the current load step,  $t$ , is extracted in three DOFs: translation in the  $x$ - and  $y$ -direction along with rotation around the  $z$ -axis, cf. Fig. 2 and eq. (2).

To eliminate the effect of compliance in the load train, a *DIC Compensator* is applied. The in-plane displacement of the shared boundary is tracked by DIC in (2) through three measurement points named: MP7, MP8 and MP9 cf. Fig. 5. The measured displacement is compared with the previous displacement  $\underline{d}_{com}(t-1)$  and the deviation,  $\underline{d}_{err}(t)$ , derived, eq. (3). This deviation is added to  $\underline{d}_{num}(t)$  to find the compensated displacement at the current load step  $\underline{d}_{com}(t)$ , eq. (4).  $\underline{d}_{num}(t)$ ,  $\underline{d}_{com}(t)$  and  $\underline{d}_{err}(t)$  contains  $x$ - and  $y$ -translation and  $z$ -rotation in the format of eq. (2). This compensator is similar to the one used in [16] except here, only the subsequent command signal is updated instead of iterating several times for every step. The corresponding displacement of actuator A, B and C,  $\underline{d}_{act}(t)$  eq. (1) is derived through a trigonometric algorithm following the assumption of rigid body motion in (3).

$$\underline{d}_{act}(t) = [d_A(t) \ d_B(t) \ d_C(t)] \quad (1)$$

$$\underline{d}(t) = [y(t) \ x(t) \ \varphi(t)] \quad (2)$$

$$\underline{d}_{err}(t) = \underline{d}_{com}(t-1) - \underline{d}_{num}(t-1) \quad (3)$$

$$\underline{d}_{com}(t) = \underline{d}_{num}(t) + \underline{d}_{err}(t) \quad (4)$$

Through (4) the current compensated displacement  $\underline{d}_{com}(t)$  is transferred to a digital PID controller in (5) operated in displacement mode. Here an electrical command signal  $\underline{i}_c(t)$  is generated and passed to the servo valves in (6) causing the actuator to move  $\underline{d}_{act}(t)$  and apply reaction forces on the test specimen. These reaction forces  $\underline{R}(t)$ , eq. (6), is obtained by load cells in (7) and transferred to the numerical substructure through (8-10). Further details of the experimental substructure are outlined in Fig. 5.

Through (7) the restoring force for the current load step  $\underline{R}_{act}(t)$ , i.e. the reaction force from the test specimen in the shared boundary, is acquired. The forces in the actuators  $\underline{R}_{act}(t)$  is transformed into section forces in the shared boundary  $\underline{R}(t)$  through a trigonometric calculation in (9), assuming a rigid connection. In a hybrid simulation the restoring force from the experimental substructure is one step behind the numerical simulation [24] – referred to here as communication delay. This is compensated for by a *Communication Delay Compensator*. In (10) the restoring force for the upcoming load step  $\underline{R}(t+1)$  is extrapolated through a Least-Square linear regression. The restoring forces in the up-coming load step,  $\underline{R}(t+1)$  is extrapolated by the 4 or 3 previous restoring forces as function,  $\psi$ , of the previous external displacements, eq. (7).

$$\underline{R}_{act}(t) = [R_A(t) \ R_B(t) \ R_C(t)] \quad (5)$$

$$\underline{R}(t) = [V(t) \ H(t) \ M(t)] \quad (6)$$

$$R_V(t+1) = \psi(R_V(t-m), D_{ext}(t-m), R_V(t-m+1), D_{ext}(t-m+1), \dots, R_V(t), D_{ext}(t)) \text{ for } m = 3,4 \quad (7)$$

$$R_H(t+1) = \psi(R_H(t-m), D_{ext}(t-m), R_H(t-m+1), D_{ext}(t-m+1), \dots, R_H(t), D_{ext}(t)) \text{ for } m = 3,4 \quad (8)$$

$$R_M(t+1) = \psi(R_M(t-m), D_{ext}(t-m), R_M(t-m+1), D_{ext}(t-m+1), \dots, R_M(t), D_{ext}(t)) \text{ for } m = 3,4 \quad (9)$$

## Test Result

A GFRP beam is tested in a quasi-static single component hybrid simulation setup presented in Fig. 2 and Fig. 5. A test of the emulated structure is conducted for verification purposes cf. Fig. 1 and Fig. 7. The system is loaded with a ramped deformation pattern in the range: 0.0mm to 6.5mm which is equivalent to a vertical reaction force of 0.0 to 5.0 KN. The load is applied through 20, 40 and 60 steps per period cf. Fig. 10 at a rate of approximately 9 sec/step.

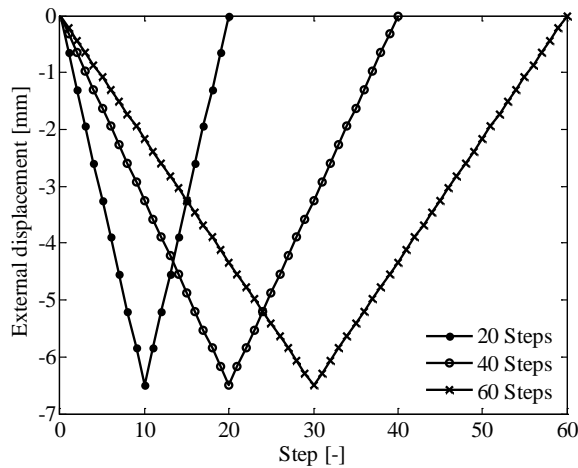


**Fig. 10 Ramped external displacement pattern for a single period**

In order to verify that both the reference test and hybrid simulation setup does not introduce out-of-plane displacements e.g. twisting, both sides of the GFRP beam is monitored in the measurement points stated in Table 4.

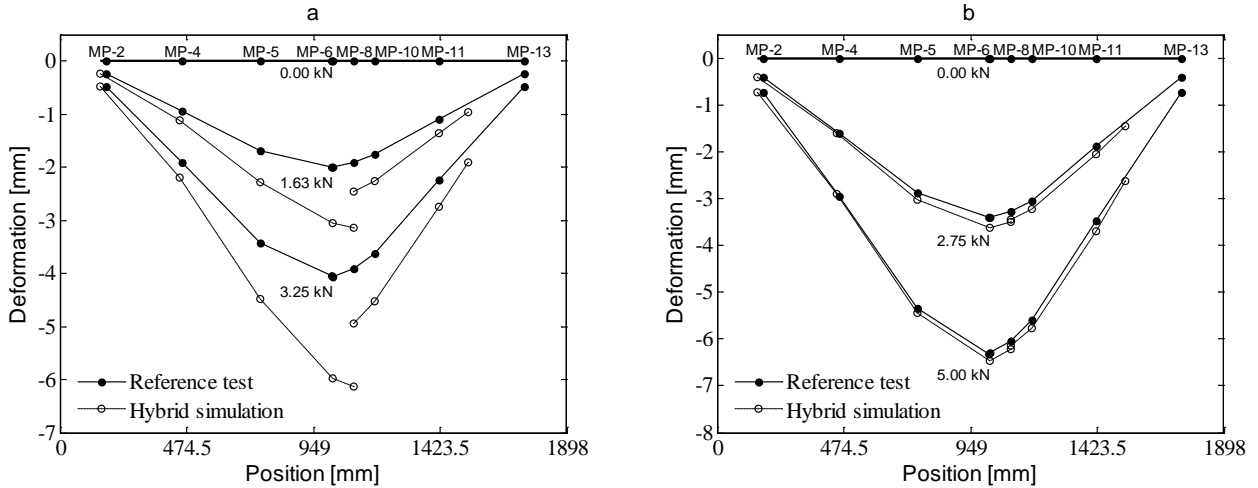
**Table 4 Error for in-plane displacement between side 1 and 2 and out-of-plane displacements at 5kN**

|                         |                         | Numerical substructure |        |        | Experimental substructure |         |         | Mean  |
|-------------------------|-------------------------|------------------------|--------|--------|---------------------------|---------|---------|-------|
|                         |                         | MP - 4                 | MP - 5 | MP - 6 | MP - 8                    | MP - 10 | MP - 11 | -     |
| Reference Test          | Side 1 vert. [mm]       | -2.96                  | -5.34  | -6.29  | -6.05                     | -5.60   | -3.48   | -     |
|                         | Side 2 vert. [mm]       | -2.94                  | -5.46  | -6.36  | -6.13                     | -5.67   | -3.49   | -     |
|                         | Dev. vert. [mm]         | 0.01                   | 0.12   | 0.07   | 0.08                      | 0.07    | 0.01    | 0.060 |
|                         | Side 1 hor. [mm]        | 0.138                  | 0.133  | 0.128  | 0.144                     | 0.137   | 0.117   | -     |
|                         | Side 2 hor. [mm]        | 0.124                  | 0.157  | 0.133  | 0.146                     | 0.118   | 0.126   | -     |
|                         | Dev. Hor. [mm]          | 0.014                  | 0.024  | 0.005  | 0.002                     | 0.019   | 0.009   | 0.012 |
| Hybrid simulation       | Out-of-plane disp. [mm] | 0.05                   | 0.04   | 0.04   | 0.04                      | 0.03    | 0.02    | -     |
|                         | Side 1 vert. [mm]       | -                      | -      | -      | -6.04                     | -5.64   | -3.59   | -     |
|                         | Side 2 vert. [mm]       | -                      | -      | -      | -6.25                     | -5.83   | -3.76   | -     |
|                         | Dev. vert. [mm]         | -                      | -      | -      | 0.21                      | 0.19    | 0.17    | 0.190 |
|                         | Side 1 hor. [mm]        | -                      | -      | -      | 0.080                     | 0.100   | 0.100   | -     |
|                         | Side 2 hor. [mm]        | -                      | -      | -      | 0.100                     | 0.112   | 0.121   | -     |
| Dev. Hor. [mm]          | -                       | -                      | -      | 0.020  | 0.012                     | 0.021   | 0.018   |       |
| Out-of-plane disp. [mm] | -                       | -                      | -      | 0.02   | 0.00                      | 0.04    | -       |       |

The numerical substructure represented in Table 4 is not considered, since no out-of-plane deformations are observed. It is noted that the out-of-plane displacements are of a magnitude equal to the measurement precision cf. Table 3 and therefore insignificant. A deviation of vertical and horizontal displacement between side 1 and 2 are clearly identified for the hybrid simulation, probably induced by misalignment of the load train. The same effect are also identified in the reference test, however the magnitude are significantly smaller. The deviation between the vertical and horizontal displacement of both sides of the specimen are proportional to the load.

### Digital Image Correlation Compensator

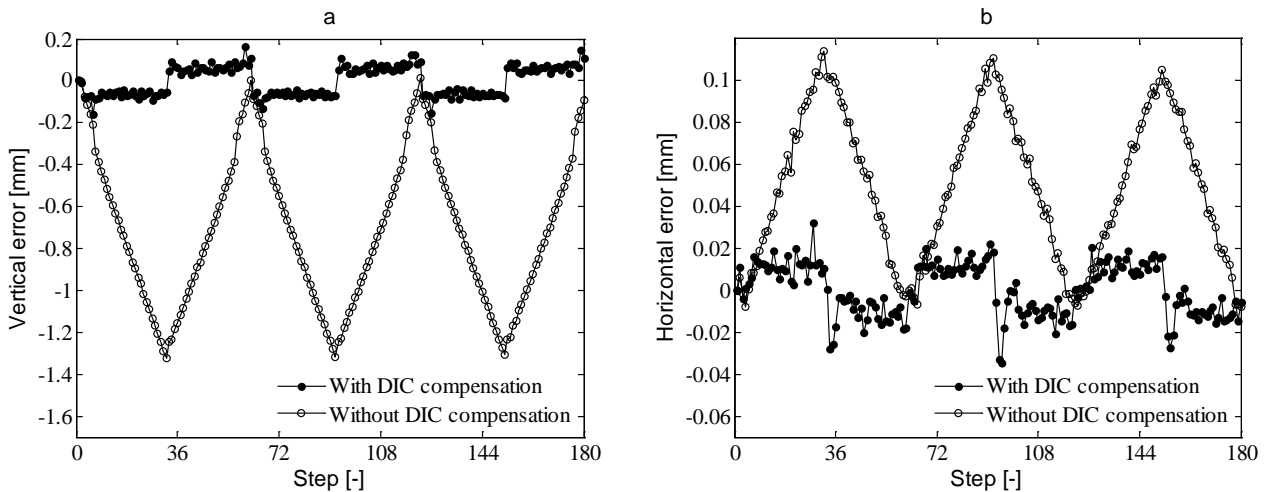
By the use of 60 steps per loading period, the difference between enabling and disabling DIC compensation is investigated, cf. eq. (3).



**Fig. 11 Displacement distribution of GFRP beam: (a) DIC compensation disabled and (b) DIC compensation enabled**

From Fig. 11a the displacement distribution of the hybrid simulation reveal a significant lack of bending stiffness relative to the reference test along with a discontinuity in the shared boundary of 33% due to compliance in the load train. However when using the DIC system to compensate for these effects, the reference test and hybrid simulation correlates significantly better with a maximum deviation of 2.6% relative to the reference test cf. Fig. 11b. The DIC compensator slowed the program by 50ms per step.

The deviation between the numerical and experimental substructure is presented in Fig. 12 including: vertical, horizontal and rotational error at the shared boundary. For all three degrees of freedom the effect of DIC compensation is significant.



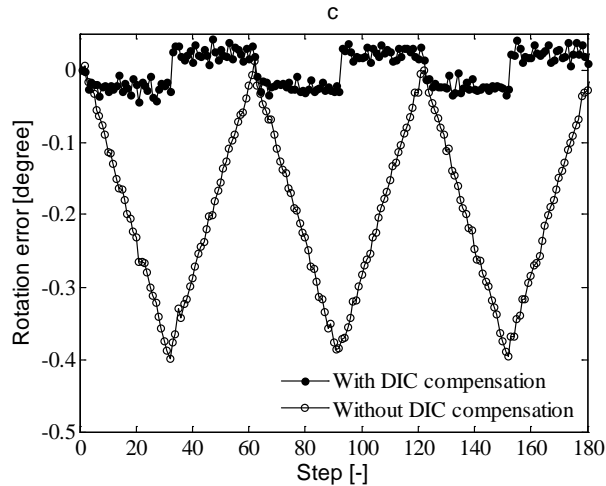


**Fig. 12: deviation between cmd and feedback signal at shared boundary: (a) vertical, (b) horizontal and (c) rotation**

The error between the numerical and experimental substructure in the shared boundary were decreased by 89% for rotations and 87% for vertical- and 69% for horizontal displacements.

#### Communication Delay Compensator

With 20 steps per loading period, compensation of the communication delay is performed through linear regression of the restoring force, eq. (7)-(9). Two different compensator schemes is implemented: “no comp” where the restoring force to the current external displacement is set equal to the previous and “linear” where the restoring force is extrapolated by least-square linear regression from the previous three or four measurement points.

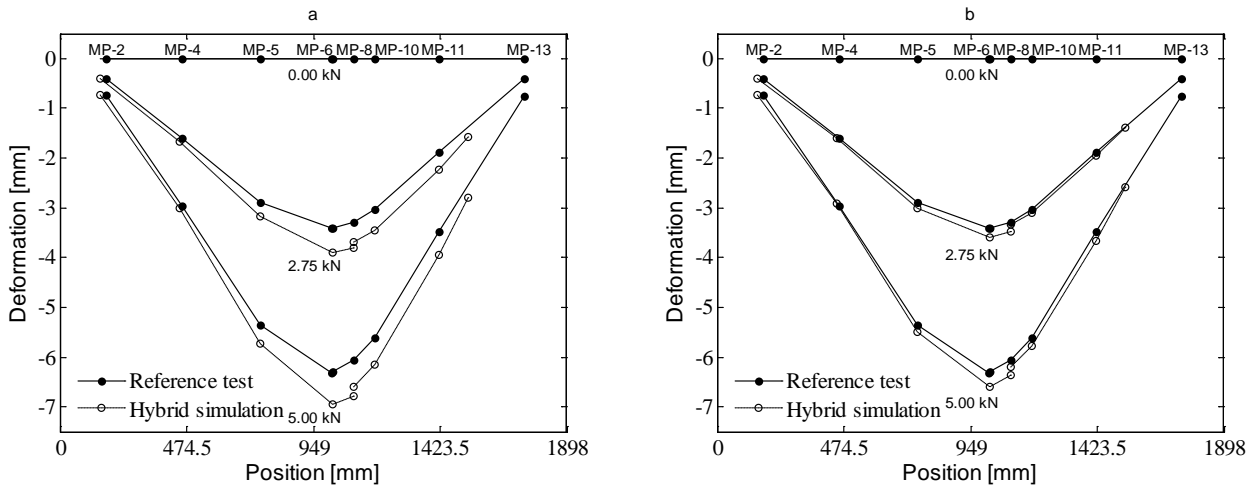


**Fig. 13 Displacement distribution with 20 sub-steps per period: (a) no compensator and (b) 4 point linear compensator**

From Fig. 13a the displacement distribution of the hybrid simulation reveal a lack of bending stiffness with a maximum deviation of 9.3%, relative to the reference test. However, when a 4 point linear compensator is implemented the reference test and hybrid simulation correlate with a maximum deviation of 4.6% relative to the reference test cf. Fig. 13b.

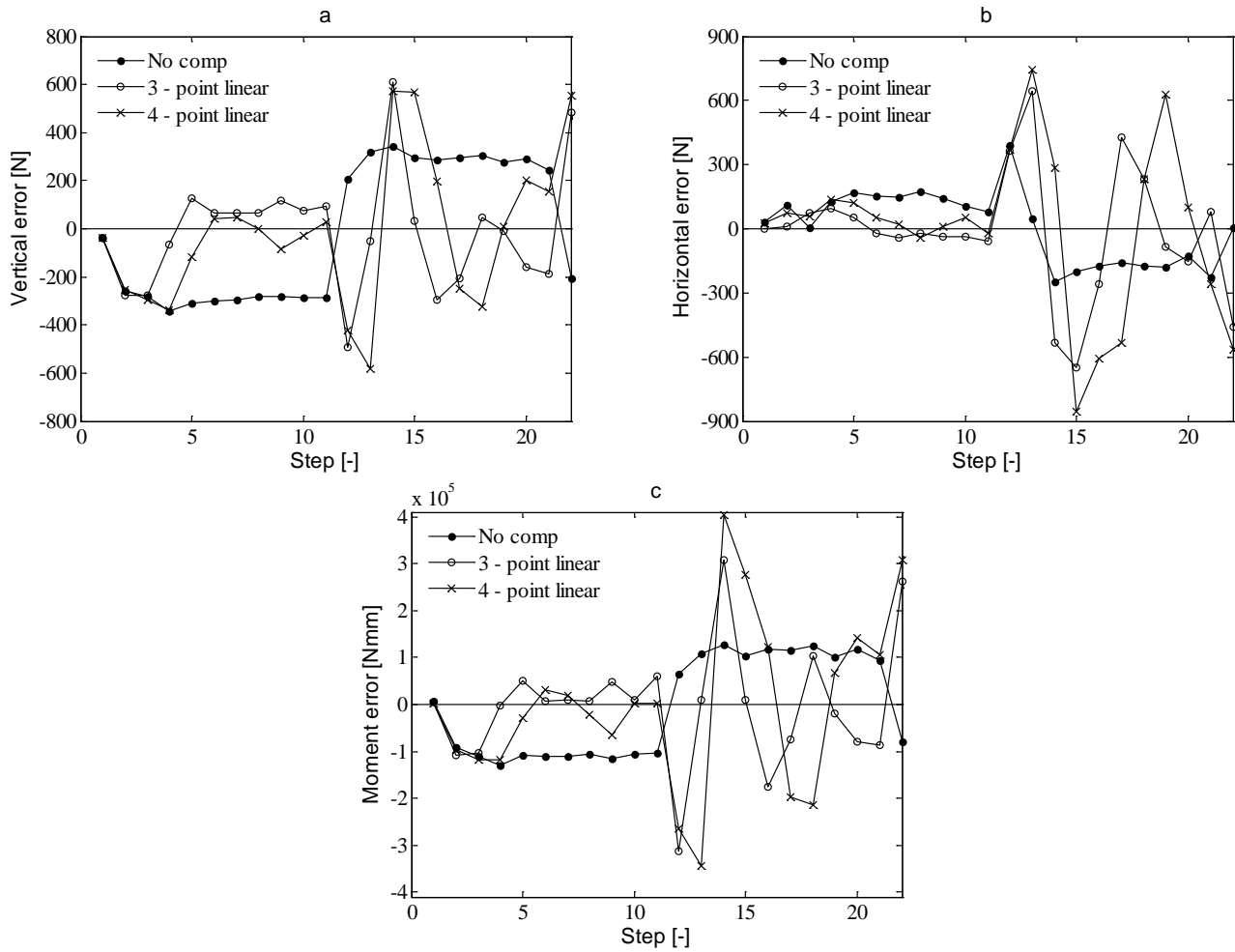


**Fig. 14** Deviation between predicted and given restoring force at 20 steps per period: (a) vertical, (b) horizontal and (c) moment

The deviation between the compensated and given restoring force is presented in Fig. 14 for: vertical, horizontal and moment error. For all three degrees of freedom, the effect is significant within the first 11 steps. However, when the external displacement changes direction, instability is introduced by the compensator which will converge during a number of steps. Within the first half loading period, the averaging error in all three DOFs is presented for 20, 40 and 60 steps per period in Table 5.

**Table 5** Average vertical, horizontal and rotational error at first half loading period

| Steps per period | Compensator type | Avg. vertical error [N] | Relative dev. [%] | Avg. horizontal error [N] | Relative dev. [%] | Avg. moment error [Nmm] | Relative dev. [%] |
|------------------|------------------|-------------------------|-------------------|---------------------------|-------------------|-------------------------|-------------------|
| 20               | Non              | -269                    | -                 | 113                       | -                 | -98900                  | -                 |
|                  | 3 point linear   | -41                     | 15.4              | 22                        | 19.5              | -19465                  | 19.7              |
|                  | 4 point linear   | -94                     | 34.9              | 45                        | 39.8              | -35563                  | 35.9              |
| 40               | Non              | -141                    | -                 | 66                        | -                 | -52286                  | -                 |
|                  | 3 point linear   | -22                     | 15.6              | 11                        | 16.7              | -8457                   | 16.2              |
|                  | 4 point linear   | -25                     | 17.7              | 11                        | 16.7              | -9334                   | 17.9              |
| 60               | Non              | -96                     | -                 | 50                        | -                 | -35581                  | -                 |
|                  | 3 point linear   | -21                     | 21.9              | 11                        | 22.0              | -7931                   | 22.3              |
|                  | 4 point linear   | -11                     | 11.5              | 7                         | 14.0              | -4084                   | 11.5              |

From Table 5 the deviation between the compensated and given restoring force decreases significantly when using a linear compensator within the first half loading period.

### Combined Effect of Compensators

By the use of a 4 point linear compensator eq. (7), 60 steps per loading period and DIC compensation eq. (3), the hybrid simulation method is compared with the reference test including: strain and displacement measurements.

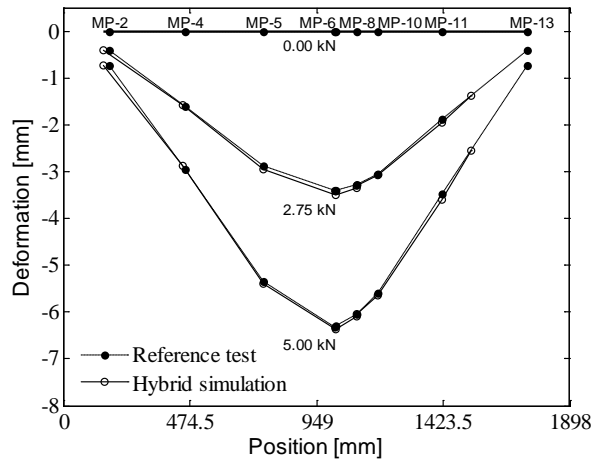


**Fig. 15 Displacement distribution of GFRP beam including: test, hybrid simulation and FE-model**

In Fig. 15 the displacement distribution in the reference test and hybrid simulation is shown, measured in the measurement points (MP) stated in the top part of the graph. The maximum deviation between the reference test and hybrid simulation is 2.1% relative to the reference test.

The vertical and horizontal displacement and rotation of the shared boundary are measured through MP - 7, MP - 8 and MP - 9 for both the reference test and hybrid simulation of the experimental and numerical substructure cf. Fig. 16. A good correlation between the hybrid simulation and reference test is identified in terms of vertical and rotational stiffness of the shared boundary. In the horizontal direction, a deviation in stiffness is identified between the reference test and hybrid simulation. In Fig. 16c, an offset between the reference test, numerical- and experimental substructure is identified. In the reference test, this offset is likely due to contact issues in the loading nose. Since the numerical and experimental substructure represents the command (cmd) and feedback signal respectively, this offset may be due to compliance in the load train.

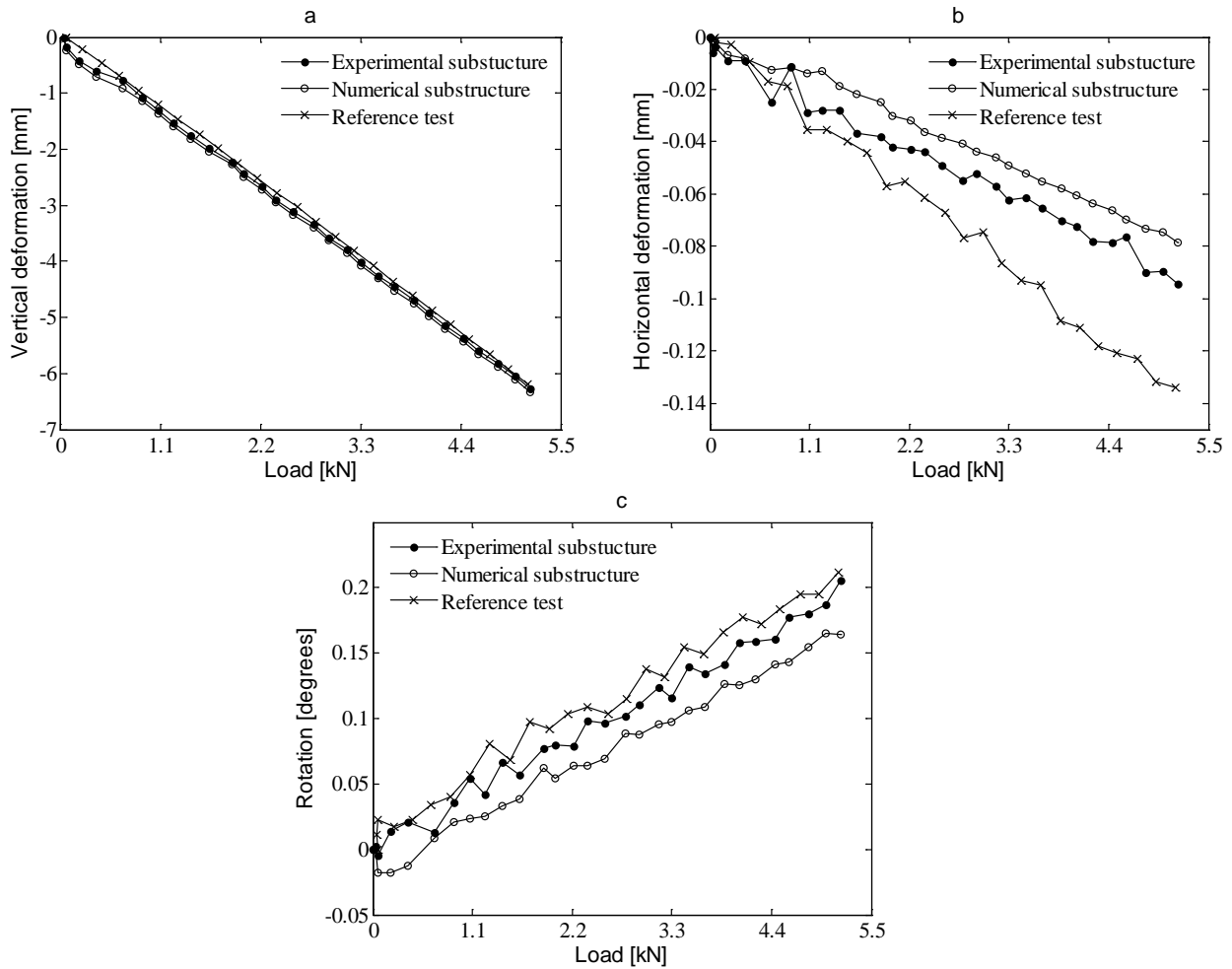


**Fig. 16 Displacement of the shared boundary: (a) vertical, (b) horizontal and (c) rotation**

The strain distribution of the top and bottom flange is compared between the reference test and hybrid simulation through a number of strain gauges mounted on the experimental sub structure; see Fig. 5 and Fig. 6.

For SG-3t, SG-4t and SG-5t represented in Fig. 17b some non-linear effects is observed due to the initiated slits in the top flange of the GFRP beam. The relative maximum deviation between the reference test and hybrid simulation is here found to be 47% for SG-3t, 17% for SG-4t and 6.2% for SG-5t, relative to the reference test.

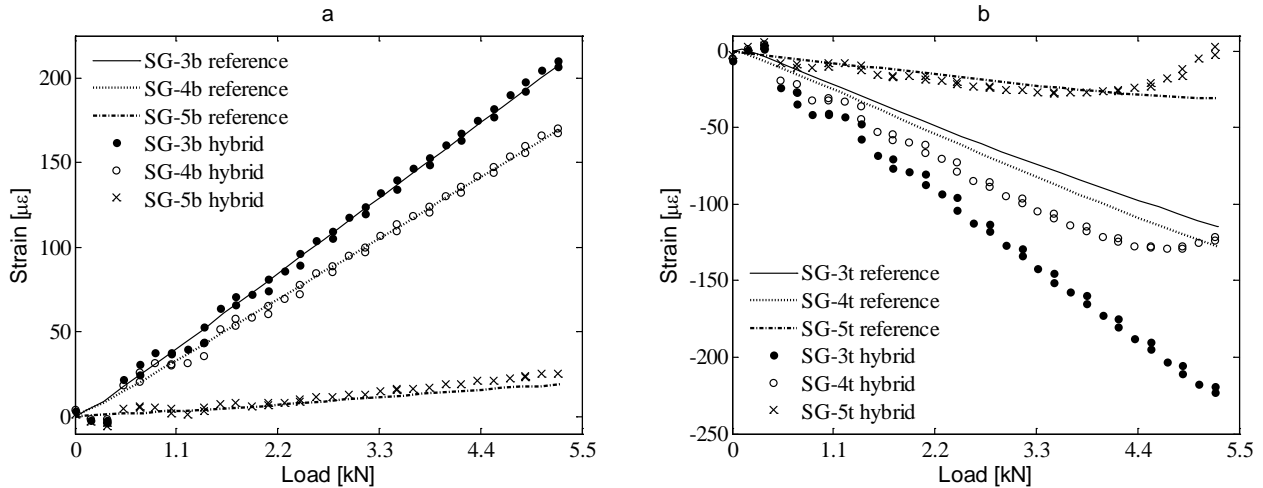


**Fig. 17 strain gauge measurements at the experimental substructure: (a) bottom flange and (b) top flange**

All strain gauges in the bottom flange reveal a linear response. For SG-3b, SG-4b and SG-5b represented in Fig. 5b the maximum deviation between the reference test and hybrid simulation is found to be 2.3%, 0.7% and 2.4% respectively, relative to the reference test.

## Discussion

The overall response of the hybrid simulation was coinciding with the reference test within maximum 2.1%, when using a 4-point linear compensator and DIC compensation for displacement adjustment. This proved the hybrid simulation setup was capable of performing an accurate simulation of the compliance behavior of the composite beam. Some discrepancies between the two were observed and these will be discussed in the following. The main topics are: discrepancies between the two sides of the beam, the strains in the top and bottom flanges and the effects of the compensator schemes.

A discrepancy between the deflections of the two sides of the beam was observed. For the reference test, the deviation was in average  $60\mu\text{m}$  and  $12\mu\text{m}$  for the vertical and horizontal displacement. For the hybrid simulation the deviation was  $190\mu\text{m}$  and  $18\mu\text{m}$  for vertical and horizontal displacement, cf. Table 4. This indicates some out-of-plane effects in the test rig connecting the actuators to the specimen. One can argue whether to fix the actuators against out-of-plane movements to minimize these errors. However, all specimens have some out-of-plane imperfections that might introduce the observed out-of-plane displacements and if the test rig is constraining this, it might initiate undesired damage to the specimen and load train instead of letting it distort freely.

The deviation in strains between the hybrid simulation and the reference test was maximum 47% - found on the top-flange, closest to the loading nose. This deviation is most likely caused by stress concentrations introduced by the point load applied in the reference test. The two remaining strain gauges at the top-flange indicated a nonlinear strain induced by buckling (cf. Fig. 17b) in the hybrid simulation, which was not the case in the reference test. It is not clear why buckling was introduced before in the hybrid simulation than in the reference test. However, buckling is induced by small imperfections in the geometry, layup, cutting of the slit etc. and these might vary greatly from specimen to specimen. However, the different buckling behavior is not important in relation to the performance of the hybrid simulation, since this primarily

depends on the ability of obtaining the correct overall response and transferring the DOFs correctly in the shared boundary.

The DIC compensation technique showed a significant improvement of the beam's overall deflection, with a deviation between the reference test and hybrid simulation going from 33% to 2.6%, cf. Fig. 11, while slowing the step speed by 50ms. This is because the deformations and slack in the test fixture, see Fig. 5, are not accounted for when disabling the DIC compensation. This also means, that the error between the numerical and experimental substructure in the shared boundary could be decreased by 89% for rotations and 87% for vertical- and 69% for horizontal displacements, cf. Fig. 12. This proved that using DIC in an outer control loop to operate the shared boundary is an efficient strategy.

The accuracy of the hybrid simulation was improved through compensation of communication delay. This was done by linear regression, using 3 and 4 previous data points. The 4 point compensator was capable of improving the overall deflection response of the beam from 9.3% to 4.6% cf. Fig. 13. The accuracy of compensator was evaluated by comparing the predicted restoring force with the actual restoring force, cf. Fig. 14 and Table 5. For both force and moment the compensator improved the accuracy for the first half period of the loading sequence. But, when the external displacement changes direction the accuracy of the compensator diminished.

## **Conclusion**

A static single-component hybrid simulation of a composite beam was performed and the results were compared to the reference test. In these tests high correspondence between the hybrid simulation and the reference test was observed, when comparing the overall displacement response along the shared boundary cf. Fig. 15 and Fig. 16. This verifies the hybrid simulation as a sub structural testing technique for the given configuration. This also shows that comparing the hybrid simulation with a reference test is a powerful tool when evaluating hybrid simulation; however in larger structures this is not feasible.

In order to increase the accuracy of the physical specimen's stiffness response, communication delay were compensated through linear extrapolation of the previous restoring force as function of external displacement. This increased the accuracy by 2.1%. Furthermore, the deviation between the numerical- and experimental substructure was improved by adjusting the displacement through DIC compensation. This technique improved the accuracy of the vertical, horizontal displacement and rotation by 87%, 69% and 89% respectively. This DIC compensator also improved the accuracy of the overall displacement shape from 33% to 2.6%. This method was introduced because of the high compliance of the load train. The higher compliance and complexity in the load train is due to the test is a single component test that requires a more comprehensive test rig to apply the desired actions in the shared boundary. This is in general not the case in multicomponent hybrid simulation where the shared boundary is simple with few DOFs.

## **Acknowledgement**

The authors would like to acknowledge the financial support from the Danish Centre for Composite Structures and Materials (DCCSM) funded by the Danish Council for Strategic Research within Sustainable Energy and Environment (Grant 09-067212). Furthermore, the authors acknowledge Fiberline Composites for the donation of the GFRP test specimens.

## References

- [1] F. M. Jensen, B. G. Falzon, J. Ankersen and H. Stang, "Structural Testing and Numerical Simulation of a 34m Composite Wind Turbine Blade," *Composite Structures*, vol. 76, pp. 52 - 61, 2006.
- [2] F. M. Jensen, "Ultimate Strength of a Large Wind Turbine Blade," Department of Civil Engineering, Technical University of Denmark, Kgs. Lyngby, 2008.
- [3] P. Brondsted, H. Lilholt and A. Lystrup, "Composite Materials for Wind Power Turbine Blades," *Annual Review of Materials Research*, vol. 35, pp. 505-538, 2005.
- [4] S. A. Mahin, P.-S. B. Shing, C. R. Thewalt and R. D. Hanson, "Pseudodynamic test method. Current status and future directions," *Journal of Structural Engineering New York, N. Y.*, vol. 115, no. 8, pp. 2113-2128, 1989.
- [5] P. B. Shing, M. Nakashima and O. S. Bursi, "Application of pseudodynamic test method to structural research," *Earthquake Spectra*, vol. 12, no. 1, pp. 26-56, 1996.
- [6] K. Takanashi and M. Nakaschiman, "Japanese Activities on ON-LINE Testing," *Journal of Engineering Mechanics*, vol. 113, no. 7, pp. 1014-1032, 1987.
- [7] C. Chen, J. M. Ricles, T. L. Karavasilis, Y. Chae and R. Sause, "Evaluation of a real-time hybrid simulation system for performance evaluation of structures with rate dependent devices subjected to seismic loading," *Engineering Structures*, vol. 35, pp. 71-82, 2012.
- [8] A. Bonelli and O. S. Bursi, "Generalized-alpha methods for seismic structural testing," *Earthquake Engineering and Structural Dynamics*, vol. 33, pp. 1067-1102, 2004.
- [9] T. L. Karavalis, J. M. Ricles, R. Sause and C. Chen, "Experimental evaluation of the seismic performance of steel MRFs with compressed elastomer dampers using large-scale real-time hybrid simulation," *Engineering Structures*, vol. 33, pp. 1859-1869, 2011.
- [10] M. Ito, Y. Murata, K. Hoki and M. Nakashima, "Online Hybrid Test on Buildings with Stud-Type Damper Made of Slitted Steel Plates Stiffened by Wood Panels," *Procedia Engineering*, vol. 14, pp. 567-571, 2011.
- [11] A. Jacobsen, T. Hitaka and M. Nakashima, "Online test of building frame with slit-wall dampers capable of condition assessment," *Journal of Constructional Steel Research*, vol. 66, pp. 1320-1329, 2010.
- [12] Y. Z. Lin and R. E. Christenson, "Comparison of Real-time Hybrid Testing with Shake Table Test for an MR Damper Controlled Structure," *American Control Conference*, pp. 5228-5233, 2009.
- [13] J. E. Carrion, B. F. Spencer Jr. and B. M. Phillips, "Real-Time Hybrid Testing of a Semi-Actively Controlled Structure with an MR Damper," in *American Control Conference*, Hyatt Regency

Riverfront, St. Louis, MO, USA, 2009.

- [14] X. Shao, A. M. Reinhorn and M. V. Sivaselvan, "Real-Time Hybrid Simulation Using Shake Tables and Dynamic Actuators," *Journal of Structural Engineering*, vol. 137, no. 7, pp. 748-760, 2011.
- [15] C. Chen, J. M. Ricles, T. M. Marullo and O. Mercan, "Real-time hybrid testing using unconditionally stable explicit CR integration algorithm," *Earthquake Engineering and Structural Dynamics*, vol. 38, pp. 23-44, 2009.
- [16] J. Waldbjørn, J. Høgh, J. Wittrup-Schmidt, M. Nielsen, K. Branner, H. Stang and C. Berggreen, "Strain and Deformation Control by Fibre Bragg Grating and Digital Image Correlation," *Strain*, 2013.
- [17] X. Fayolle, S. Galloch and F. Hild, "Controlling Testing Machines with Digital Image Correlation," *Experimental Techniques*, vol. 31, no. 3, pp. 57-63, 2007.
- [18] J. Waldbjørn, J. Høgh, C. Berggreen, J. Wittrup-Schmidt and K. Branner, "Hybrid Testing of Composite Structures with Single-axis Control," in *The 19th International Conference on Composite Materials*, Montreal, Canada, 2013.
- [19] ASTM, Standard Test Method for Tensile Properties of Polymer Matrix Composite Materials, West Conshohocken, Pennsylvania, United States of America: ASTM International, 2011.
- [20] ASTM, Standard Test Method for Shear Properties of Composite Materials by the V-Notched Beam Method, West Conshohocken, Pennsylvania, United States of America: ASTM International, 2014.
- [21] R. Bitter, T. Mohiuddin and M. Nawrocki, *LabView Advanced Programming Techniques*, Boca Rotan, Florida, USA: CRC Press, 2001.
- [22] N. Instruments, "<http://www.ni.com/pdf/manuals/373781e.pdf>," National Instruments, 8 2009. [Online]. [Accessed 12 11 2014].
- [23] N. Instruments, "<http://www.ni.com/pdf/manuals/374188d.pdf>," National Instruments, 2 2008. [Online]. [Accessed 12 11 2014].
- [24] E. C. Juan and F. S. J. Billie, *Model-based Strategies for Real-time Hybrid Testing*, Urbana-Champaign: Illinois Digital Environment for Access to Learning and Scholarship - Dept. of Civil and Environmental Engineering, 2007.